Simple and eco-friendly fabrication of electrode materials and their performance in high-voltage lithium-ion batteries

Lucía Barbosa[a,1], Fernando Luna-Lama[b,1], Yarivith González Peña[a], Alvaro Caballero[b,*]

[a]Instituto de Investigación en Tecnología Química (CONICET), Facultad de Química Bioquímica y Farmacia (UNSL), Almirante Brown 1455, San Luis (D5700HGC), Argentina.

[b]Dpto. Química Inorgánica e Ingeniería Química, Instituto Universitario de Nanoquímica, Universidad de Córdoba, 14071, Córdoba, Spain.

[1]These authors contributed equally to this work.

*Correspondence: alvaro.caballero@uco.es (A.C.); Tel.: +34957218620

Abstract

The huge consumption of rechargeable Li-ion batteries (LIBs) make it necessary to recover and reuse the different components of spent batteries, thus favouring sustainable development. Graphite is a critical material in the manufacture of the current LIBs so recycling it should be prioritized in the management of spent batteries. In this work, graphite was manually recovered from spent batteries used in smartphones. The impurities from the different components of the batteries were drastically reduced by simple leaching with HCl. This treatment significantly improved the delivered specific capacity, with an average value of 300 and 390 mAh g^{-1} without and with leaching, respectively. To test recycled graphite as anode material in real cells, it was paired with $LiNi_{0.5}Mn_{1.5}O_4$, the most promising cathode material for high-voltage batteries. As a novelty, LiCl, produced directly via the chlorination process of spodumene, was used as Li source to obtain the spinel sample. The real cell showed satisfactory values of both the initial specific capacity (100 mAh g^{-1}) and the capacity retention after 100 cycles. These results are comparable to and in some cases even better than those of cells that use commercial graphite and conventional Li sources as primary raw materials. Moreover, the cell showed a good performance during the rate capability test, where the delivered capacity values decreased smoothly from 73 to 62 mAh g^{-1} while the rate increased from 0.1C to 1C, respectively.

Keywords: spent batteries; recycled graphite; LNMO spinel; high-voltage; full cell Li-ion

Introduction

Forthcoming banning of fossil fuel vehicles will boost the mass production of electric vehicles (EVs). In this context, the next challenge will be to manufacture affordable EVs for worldwide users by lowering production costs. Most EVs are powered by rechargeable batteries, mainly lithium-ion batteries (LIBs).[1] This and other conventional and emerging sectors, such as smart devices, renewable energy storage, and automation of equipment in industry, will be responsible for a predictable spectacular increase in demand and, hence, for the expected Li-ion battery market growth to $92.2 billion by 2024. In 2018, sales were around $37.4 billion, which means an annual growth rate of more than 16 %. The spectacular increase in consumption will involve tremendous growth in spent LIBs. This growth is predicted to stand for 11 millions of tons of spent LIBs by 2030.[2] Spent LIBs are composed of diverse materials: 31% cathode material, e.g. $LiCoO_2$, $LiMn_2O_4$, $LiFePO_4$, as well as other metal oxides; 8% aluminium; 22% anode material, e.g. graphite; 17% copper; 15% organic electrolytes; 3% membrane separator; 4% carbon black and binder, e.g. PVDF.[2] The recycling of these waste batteries is not only beneficial from an economic point of view because of the valuable materials they contain but also an imperative in harmony with sustainable development since they are considered hazardous waste due to the presence of toxic metals and corrosive electrolytes.[3]

Two of the key functional constituents of LIBs are present in the positive and negative electrodes, i.e. cathode and anode materials. Most marketed LIBs use mixed oxides of Li and other metallic elements (Co, Ni, Mn, and Al) as the cathode material. Other compounds such as $LiFePO_4$ are cheaper and more benign towards the environment, but they provide lower voltages, so their use is more limited. The anode is less versatile in terms of materials used. In commercial batteries, the only material currently used is carbon (C) in the form of graphite. Promising alternative systems include Si, but its use is so far very limited.[4] Indeed, around 1.2 million tons of graphite were used in the manufacture of LIBs. Only in electric vehicles, the consumption was 40000 tons, about 30 %

higher than the three previous years.[5] In fact, demand for raw material graphite in battery applications is forecast to grow by 17-23 % per year between 2017 and 2027. These figures constitute a powerful argument to recycle and reuse graphite from spent batteries, a subject that has received less attention than the recycling of cathode components. To our knowledge, in the last two years, five reviews [6–10] have reported on the recycling of LIBs in which more than 90 % of the content involved the recovery of the cathode components. By contrast, only one review, published in 2016 [11], deals in depth with anode recycling. In our opinion, recycling and reusing graphite from spent batteries are as important as recycling and reusing the cathode component within the so-called "circular economy" aimed at minimizing waste and making the most of resources.[12]

In this article, we focus on different strategies to lower the cost of electrode materials and combine the optimized materials to evaluate their electrochemical performance in half- and full-cell configurations. The cathode was synthesized using both a low-cost lithium reagent and a simple, cost-effective procedure. The studied material was the spinel $LiNi_{0.5}Mn_{1.5}O_4$ (LNMO) because of its theoretical specific energy (658 Wh kg^{-1}), which is greater than today's commercial cathode materials.[13] This value is based on the combination of both a high working potential (4.7 V), arising from the oxidation reaction of nickel from Ni^{2+} to Ni^{4+}, and a high specific capacity (146.7 mAh g^{-1}) delivered by the spinel structure.[14] LMNO is mainly prepared via three different routes: wet chemistry, solid-state, and molten salt methods, conventional solid-state being the simplest and most cost-effective.[15] This procedure involves the mixing of reactant powders followed by two different thermal treatments: a synthesis and an annealing step.[16,17] To date, Li_2CO_3, LiOH, and $Li(CH_3COO)\cdot 2H_2O$ have been used as the main lithium precursors.[18–25] We propose to use LiCl as a lower-cost lithium source, obtained from β-spodumene in previous investigations[26] to advance from the mineral to an end-use application. Furthermore, a one-step heat treatment is proposed to save energy consumption.

The strategy to prepare the anode material was based on the reuse of graphite from spent LIBs so as to avoid waste accumulation. Accordingly, we decided to focus our research on graphite as anode material. Currently, natural graphite is processed to prepare graphite for LIBs application. This process involves multi-step and physicochemical and mechanical procedures aimed at upgrading carbon purity and rolling of the graphite material.[11] The carbonaceous material contained in the anode of waste batteries has great potential for becoming a cost-effective raw material to prepare battery-grade graphite since it has a high C content and a high degree of graphitization. These features may lead to cost savings in upgrading and graphitization processes. In addition, this approach paves the way for promoting urban mining and waste valorization, and it is particularly convenient for those countries with scarce or no natural graphite resources.[11] To date, only a few studies have focused on spent LIBs anode as starting material to prepare battery-grade graphite.[27–30] Four of them describe the performance of regenerated graphite as LIB negative electrode in half-cell configuration [28–30] and only one in full-cell configuration, using $LiNi_{1/3}Co_{1/3}Mn_{1/3}O_2$ as cathode material[30] The investigations of Rothermel et al.[30] are of special interest since they involved an extensive study on recycled graphite from both a structural and an electrochemical point of view. They used a commercial Li-ion battery electrochemically cycled to 70 % SOH (state of health) to generate a stage like the end-of-life condition. The graphite of a non-aged cell (100 % SOH) was used as a reference. The graphite was recovered by a laborious method,[31] using subcritical and supercritical CO_2 as a solvent to eliminate the electrolyte impurities.

Here we followed an approach staying more close to reality, by using spent mobile LIBs collected in containers located in different places of San Luis city, in Argentina. These batteries were manually dismantled to separate their different components and the sample of used graphite was obtained from the negative electrodes. We eliminated the graphite impurities using a step of calcination in N_2 followed by a conventional leaching method with HCl. The upgraded graphite was

coupled with the LMNO obtained through the process here proposed, to evaluate the electrochemical performance of both electrodes in a real high voltage Li-ion cell.

Experimental Section

Synthesis of LNMO

$LiNi_{0.5}Mn_{1.5}O_4$ powders were synthesized via a facile solid-state method. Stoichiometric amounts of $Ni(NO_3)_2.6H_2O$ and $Mn(NO_3)_2.4H_2O$ (Sigma Aldrich) were mixed with LiCl obtained from β-spodumene.[26] The latter salt was added in excess to compensate for the Li volatilization during calcination. The mixture was thoroughly ground and then calcined in a tubular alumina furnace at 800 °C in air for 1 h. The solid product obtained was washed with Milli-Q® water, filtered, and dried in an oven at 70 °C for 2 h.

Recycled graphite

Spent mobile-phone batteries were collected from recycling containers installed in different places of San Luis city, Argentina. The spent batteries were immersed in brine to be discharged and dismantled manually by separating the cathode, anode, and aluminium and plastic cases. The anode material was separated from the copper foil manually and then sieved in a vibratory sieve shaker. The powder obtained was calcined at 450 °C under N_2 atmosphere for 2 h. The calcined sample was leached with 3 M HCl (37 % w/w, Panreac) at 80 °C for 2 h, washed with distilled water until neutral pH, filtered, and dried in an oven at 70 °C for 2 h, conditions similar to those used by Guo et al.[27] Figure 1 shows the scheme of the processes followed to obtain both active materials.

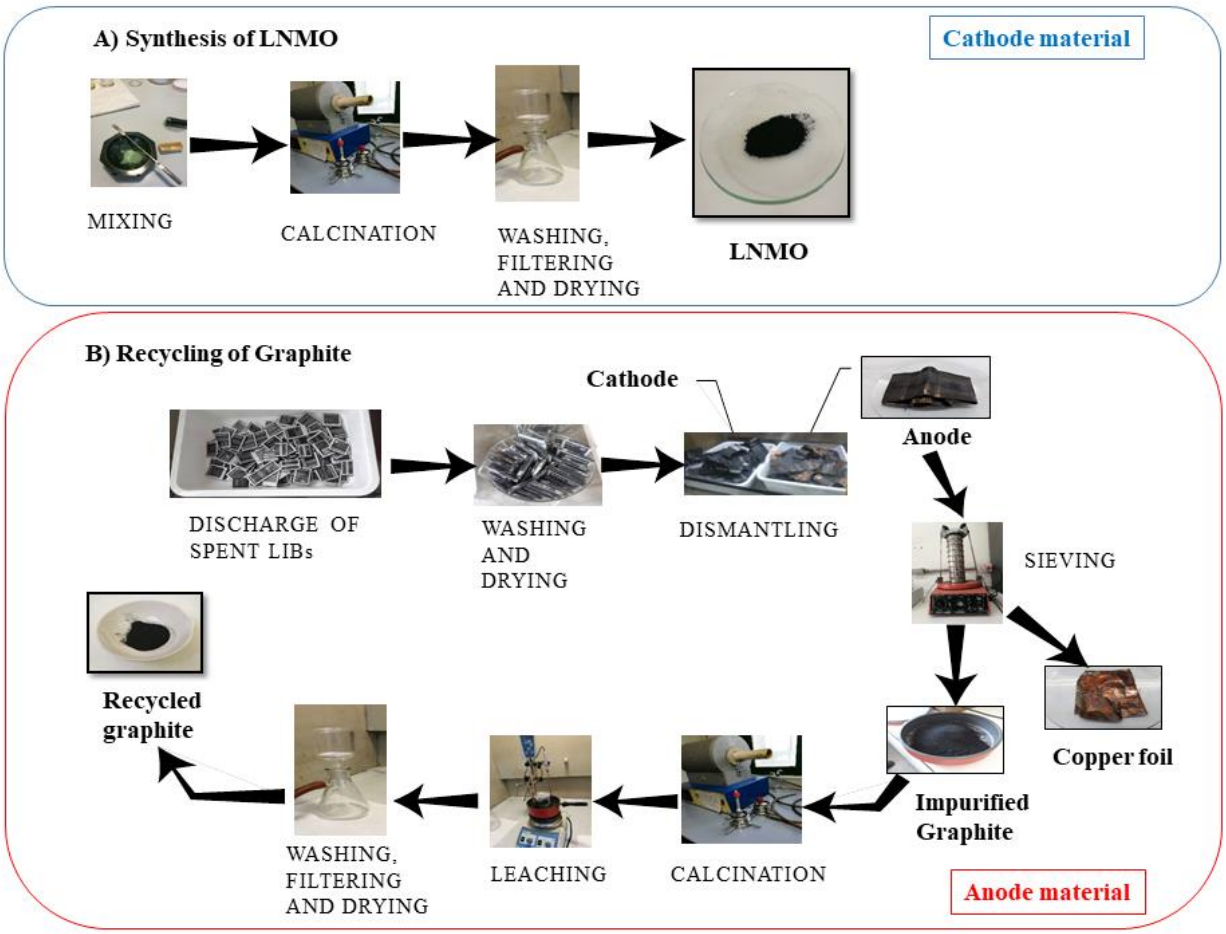

Figure 1. Scheme for LNMO synthesis and the graphite recycling process.

Characterization techniques

The composition of the recycled graphite was determined by XRF with a Primus IV spectrometer. The leachate was determined by ICP-Mass with a Perkin Elmer Nexion X apparatus. The X-ray diffraction patterns (XRD) were obtained in Bruker D8 Discover X-ray diffractometer with monochromatic Cu K_α radiation (λ = 1.5406 Å). The patterns were recorded within the 10–90º (2θ) range, using a step size of 0.02º and 7 s per step. The X-ray photoelectron spectroscopy (XPS) measurements were carried out with a PHOIBOS 150 MCD spectrometer using monochromatic Mg K_α radiation and a multichannel detector. Raman spectra were recorded with a confocal Raman spectrometer alpha500, WITec. A frequency doubled Nd:YAG laser at 532 nm (second harmonic generation) was used for excitation. The laser beam was focused on the sample using a 20x/0.4 Zeiss objective. Raman spectra were measured with an integration time of 1 second, by averaging a

total of 10 spectra. Thermogravimetric measurements were made using a Mettler Toledo-TGA/DSC under oxygen atmosphere by heating the sample from 25 to 600 ºC at 5 ºC min^{-1}. Sample morphology was investigated with a JEOL JSM-7800F scanning electron microscope (SEM) equipped with a X-ACT Cambridge Instrument detector for EDX analysis.

Preparation of electrodes and assembly of the cells

The active material, either LNMO or recycled graphite, was mixed in a mortar with carbon black and PVDF in the ratio 80:10:10 by weight. Approximately 9 mL NMP was added dropwise to the mixture and the slurry formed was maintained under stirring for 24 h at 300 rpm. The doctor blade technique was applied to spread the slurry over the substrate of 454 µm thickness GDL (gas diffusion layer, ELAT LT 1400, FuelCellStore) to fabricate the cathode and 9 µm thickness Cu foil to fabricate the anode. The choice of GDL as a current collector was based on its better performance compared to the Al in Li cells of different chemical processes.[32,33] Slurry coated foils were dried in an oven overnight at 50 °C. The dried deposits were punched with a manual punching machine into 13 mm diameter discs for the half-cell system and 16 mm diameter discs for the full-cell system. The discs were additionally dried in a glass oven (Büchi) under vacuum for 3 h. The two-electrode coin cells, CR2032 model, were assembled in a dry argon-filled glove box (M. Braun; $H_2O \leq 1$ ppm). $LiPF_6$ (1M) dissolved in EC and DEC (1:1) was used as the electrolyte, and a 16 mm diameter fiberglass disc (Whatman) was used as the separator. A LNMO/graphite mass ratio between 3.9-4.0 was used for full-cell configurations considering the delivered specific capacity of both components in a half-cell configuration. Electrochemical charge/discharge cycling tests were carried out in an Arbin BT2143 battery test system. The specific capacity values were calculated from the LNMO mass in the electrode.

Results and Discussion

Composition, structure, and morphology of Graphite

The composition of the recovered graphite was determined by XRF measurements. Table 1 shows the contents of elements found before and after leaching with HCl and subsequent washing. The Al and Cu originated from the electrode substrates; Fe from the cell case; Co and Ni and perhaps Mn from the cathode material; F and P from the electrolyte (the relationship in the non-treated sample was close to 6:1); Na from the treatment with NaCl; Si and S could be impurities from the pristine graphite. Since graphite derived from different spent LIBs, we had no data regarding its manufacturing process. The high content of impurities, especially Si and S, suggests a significant presence of natural graphite and silicone-based adhesive in the electrodes of the spent batteries.

Clearly, the leaching with HCl caused a significant decrease in the content of all the elements except for Si; some even disappeared when they were found in quantities below the detection limit of the technique (F, Na, Mn). Note the behavior of F, associated with electrolyte impurities, whose content was appreciable in the unleached graphite. After leaching, this element was below the detection limit. The high solubility of the $LiPF_6$ salt would be the cause of its drastic decrease. A small content in Cl was observed despite multiple washes carried out with distilled water. After the impurity subtraction, the C content increased from 92 to 99 %. The increase in Si content after leaching would have a similar origin, the insolubility of the phase in which it was present, probably as silicate, in HCl. The carbon content for the leached graphite was confirmed from thermogravimetric measurements carried out under dynamic oxygen atmosphere (Fig. S1). The weight loss between 400 and 800 ºC was 99.8 % assigned to the carbon combustion.

Table 1. Elemental composition of graphite recovered from spent Li-ion batteries.

Sample	C	F	Cl	O	Na	Al	Si	P	S	Li	Mn	Fe	Co	Ni	Cu
Ul*	92.3	5.5	-	-	0.06	0.04	0.07	0.75	0.15	-	0.03	0.01	0.18	69^{+}	0.93
L*	99.9	-	0.08	-	-	0.02	0.13	0.01	0.06	-	-	64^{+}	37^{+}	15.2^{+}	88^{+}
ICP-MS^{+}	-	-	-	-	38.1	10.6	-	140	-	241	8.15	3.03	44.8	2.01	219
XPS (Ul)$^{++}$	59.8	7.15	-	14.8	-	-	-	1.6	-	7.1	0.52	0.86	0.76	0.65	0.87
XPS (L)$^{++}$	94.9	-	-	5.06	-	-	-	-	-	-	-	-	-	-	-

Ul: unleached graphite; L: leached graphite; (*) XRF data in mass %; ($^{+}$) in ppm; ($^{++}$) in atomic %

Table 1 also summarizes the results of the ICP-MS measurements made to the graphite leachate. As expected, Li was the element with the highest content, involved in the charging and discharging processes of the battery and present in the electrolyte, together with P, also found in a high content; F was beyond the detection ability of the equipment used. The values of both elements were much higher than those measured by Rothermel et al.[30] in aged graphite (70 % SOH), 450 and 786 ppb, for Li and P, respectively. The origin of this difference could be due to the different aging regimes of the Li-ion batteries and to the different processes followed in the dismantling and separation of the various components. The ICP-MS values are in better tune with those reported by Yang et al.[28] whose graphite recovery process is closer to the one followed in the present work. The high content in Cu, deriving from the substrate, found by XRF, was also observed in the ICP-MS data. Finally, the higher content of Co compared with Mn and Ni, reflected in both analytical techniques, confirms that in the spent batteries Co is the majority element in the laminar oxide used as a cathode.

The XPS chemical analysis technique used was especially useful to know the composition at surface level. Figure S2 shows the XPS survey spectra of the unleached and leached graphite. Not

209 all the elements detected by XRF in the unleached sample were found in the XPS spectrum. Only
210 the elements C, O, F, P, Mn, Fe, Ni, and Cu were clearly detected, in addition to the Li, too light to
211 be measured by XRF. Table 1 summarizes the results expressed as atomic % of the detected
212 elements. Perhaps the most interesting feature of these results is the leached graphite spectrum,
213 where only the C and O elements were identified while the rest, detected by XRF, did not appear.
214 These differences were caused by the physical principles on which both spectroscopic techniques
215 are based. It is well known that the XPS is a surface technique due to its low penetration power
216 (barely few nm's in depth) whereas XRF gives information at the bulk level. As for the profile
217 shape, it is interesting to comment on the difference observed in the C 1s peak. While for the
218 leached sample, this peak (Fig. S3a) resembles that reported for graphite, a strong somewhat
219 asymmetric peak at 284.6 eV and a wide peak at 291.0 assigned to sp^2 carbon bonds and $\pi \rightarrow \pi^*$
220 (shake -up), respectively,[34] the peak asymmetry notably increases for the unleached sample (Fig.
221 S3b). A weak peak is seen around 286 eV, whose origin was assigned to C-O interactions
222 associated with products resulting from the reduction of electrolyte solvents.[35,36]

223 The XRD pattern of the unleached and leached samples exhibits the typical peaks of a highly
224 ordered graphite.[37,38] Apart from the intense and symmetrical peak assignable to the plane (002),
225 other planes of the structure corresponding to other crystallographic directions were clearly detected
226 (Fig. 2). The interlayer spacing values, $d_{(002)}$, range from 0.335-0.336 nm, consistent with that of
227 graphite (PDF 41-1487). Therefore, the impurities did not produce significant changes either in the
228 relative intensities of the peaks or in their positions.

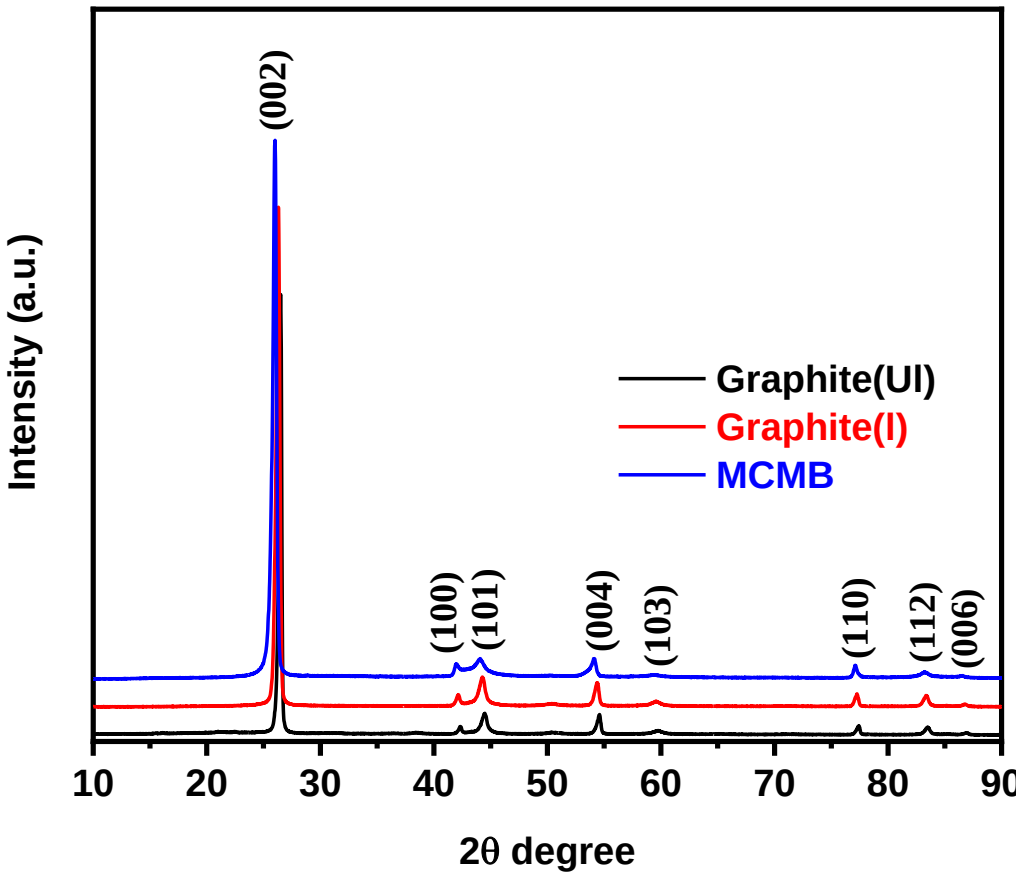

Figure 2. XRD patterns of different graphite samples.

The XRD diffraction data also provide information about particle microstructure in the form of mean crystallite dimension or size of the coherent crystalline domain and lattice imperfections (microstrains). These two quantities can be estimated from peak broadening data and are useful for quantifying material crystallinity. In this work, the contribution of microstrains and crystallite size to the peak width was determined by using the Williamson and Hall equation on the assumption of a Lorentzian peak shape:[39]

$$\beta \cos \theta = 2 \langle e \rangle \operatorname{sen} \theta + K \lambda / D \qquad (1),$$

where β is the integral breadth after correction for instrumental broadening from a highly crystalline LaB_6, $\langle e \rangle$ denotes local strains (defined as $\Delta d/d$, where d is the interplanar space), K the Scherrer constant related to the crystallite shape, and D the crystallite size. Equation (1) was applied to three order multiple reflections, (*002*), (*004*) and (*006*), and the calculated values give information along

242 <*00l*> direction, which defines the direction of the layer packing (*c* axis). This equation was applied
243 to the graphite from the spent battery before and after the leaching and to commercial graphite used
244 in the manufacture of Li-ion batteries, mesocarbon microbeads (MCMB), taken as reference
245 material. This equation is plotted in Fig. S4, and the values calculated for <e> obtained from the
246 slope and for L_c, the out-of-plane crystallite size from the intercept with K equal to 0.9[40] are shown
247 in Table 2. L_c was also calculated from the Scherrer equation (broadening resulting from crystallite
248 size alone):

249 $$D = K\lambda/\beta \cos\theta \qquad (2)$$

250 The average values obtained from the widths of the (*002*), (*004*) and (*006*) reflections are also
251 included in Table 2.

252 **Table 2.** Microstructural parameters for different graphite samples derived from their XRD
253 patterns and Raman spectra.

Graphite sample	$\langle e \rangle^{(*)}$ (10^{-3})	$L_c^{(*)}$	$L_c^{(**)}$	$L_a^{(**)}$	$L_a^{(+)}$	$L_a^{(++)}$
Unleached	1.6	108	33	69	52	26
Leached	0.6	30	24	63	166	37
MCMB	1.6	34	21	66	100	21

254 (*) Equation (1); (**) Equation (2); ($^{+}$) Equation (3); ($^{++}$) Equation (4). Values of crystallite
255 size in nm.

256 The in-plane crystallite size, L_a,[41] cannot be evaluated from XRD peak broadening using $CuK_{\alpha 1}$
257 since the (*100*) reflection overlaps with other reflections, especially with (*101*) reflection and (*101*)
258 of the rhombohedral phase, which normally coexists with the more common hexagonal phase. The
259 only reference we know in which the parameter L_a is calculated from the reflection (100) is that of
260 Cançado et al.[42] These authors used synchrotron radiation (λ = 0.120 nm) instead of the
261 conventional $CuK\alpha_1$ radiation (λ = 0.154 nm) to record the (*100*) peak. Several observations to this
262 modification of the measurement method are worth noting, namely (i) the change in radiation does

not imply the disappearance of the plane (101); (ii) if dimensions of the graphite unit cell are a = 0.2461 and c = 0.6708 nm, for a value of λ = 0.120 nm, the planes (*100*) and (*101*) should appear at 32.70 and 34.30 º (2θ), respectively, and these values are even closer than those calculated for λ = 0.154 nm, 42.36 and 44.53 º (2θ), so the overlap between both planes would continue to be present; and (iii) a probably involuntary error was observed: the peak recorded around 34.2 º (2θ) does not correspond to the plane (*100*) but to the plane (*101*). Hence, we doubt the reliability of the crystallite size L_a evaluated by these authors. The closest value to this parameter can be evaluated from (*110*) reflection, which does not overlap with any other reflection. In fact, Maslova et al.[43] used this plane to measure L_a, the crystallite diameter along the basal plane. Table 2 shows the L_a values obtained by applying equation (2) with K = 1.84.[40] These values are higher than L_c, consistent with the anisotropic properties of graphite.

Different alternative methods can be used to calculate the in-plane crystallite size, L_a, from the D and G bands of the Raman spectrum. In these methods, the values of crystallite size measured from the broadening of the diffraction planes are taken as references and graphically compared with certain properties of the bands of the Raman spectrum. Cançado et al.[42] used the controversial crystallite sizes of different graphite samples heated from 1800 to 2700 ºC to propose the following equation:

$$L_a \text{ (nm)} = (2.4 \times 10^{-10})\, \lambda^4_{laser}\, (I_D/I_G)^{-1} \qquad (3)$$

where λ is the wavelength of the laser beam used (532 nm) and I_D and I_G the intensity of the D and G bands. The I_D/I_G quotient has some shortcomings due to its dispersive character, affected not only by the wavelength but also by some doubts on how to obtain the signal intensity either by the band heights or band areas. Maslova et al.[43] found that FWHM of G band is not affected by these factors and the relationship found between this property and the crystallite size obtained from (*110*) reflection adopts the simple equation:

$$\text{FWHM}(G) = 14 + 430/L_a \qquad (4)$$

We also used equations (3) and (4) to determine the in-plane crystallite size L_a of the unleached and leached graphite (Table 2) from their Raman spectra.

As for the values of <e>, the changes are not significant, and the values are comparable to those described for commercial graphite evaluated also from XRD data using other calculation methods.[38,41] When these graphite particles are deformed either by grinding[41] or irradiation with neutrons,[38] clearly significant increases are observed; these increases can be greater than one order of magnitude. As for the values of *L*c calculated by equation (1), the one obtained for the unleached graphite, around three times that calculated for the leached graphite and MCMB, deserves attention. The values tend to equalize when the broadening of the three reflections (*00l*) is exclusively associated with the crystallite size, as in equation (2). We do not have a convincing argument to explain the abnormally low value of the intercept when equation (1) is applied to the unleached graphite, which originates the highest value of D (L_c). Considering that the three graphite samples have high crystallinity, it is acceptable to assign the broadening only to this parameter and, therefore, there is little influence of the impurities present on the crystallinity of the graphite. The limited variation of the in-plane crystallite size values, L_a, is consistent with this conclusion.

Neither of the two models used for the evaluation of L_a from Raman spectroscopy provides values comparable to those calculated from the width of the plane (*110*) reflection. The Gançado et al. method[42] gives somewhat random values for the three examined graphite samples. More homogeneity is observed in the values calculated by the Maslova et al. method.[43] Although the values are lower than those calculated by X-rays, in both characterization techniques the leaching of graphite hardly affects the value of this parameter.

We cannot confirm the results obtained by Rothermel et al.[30] about the remarkable influence exerted by the impurities on the crystallinity of graphite recycled from a Li-ion battery. These authors used Raman spectroscopy measurements to analyze the degree of graphite crystallinity using equation (3) to evaluate the in-plane crystallite size L_a, and their results are very different

from ours. The calculated value for the unwashed graphite originating from the non-aged battery was 279 nm, higher than that of the aged battery, 175 nm. When washing with CO_2 in both subcritical and supercritical conditions, the value of L_a increases considerably, even surpassing 1000 nm. In other words, the impurity decrease considerably improves the crystallinity of the graphite. We do not have a convincing explanation for this behavior, which differs greatly from that found in our graphite. We can only provide two indirect proofs that the impurities do not seem to modify the microstructure of the graphite remarkably. The first proof concerns the results of reference graphite such as the MCMB, whose microstructure is very similar to that of the graphite recovered from a spent battery, regardless of the degree of impurity. The second proof is the SEM images, which we discuss next, where no appreciable differences are observed before and after washing with HCl.

The geometrical shape of the particles, as revealed by SEM images (Fig. 3a), is that expected for this material with layered structure, micrometric flakes of different size and thickness. Leaching with HCl does not have a significant effect on the morphology and particle size (Fig. 3b).

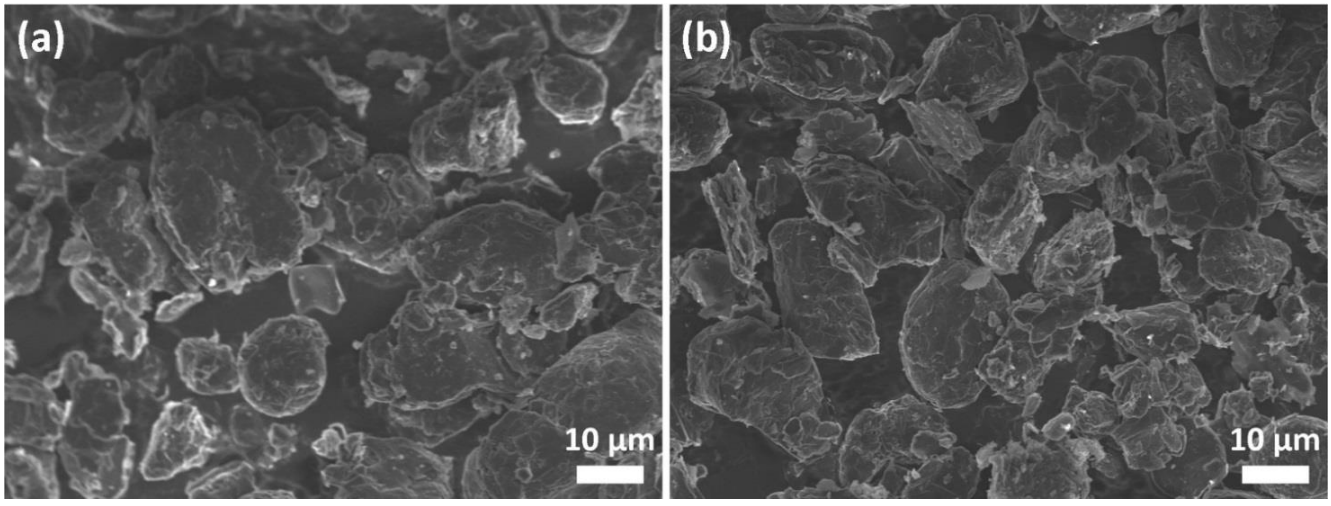

Figure 3. SEM images of unleached (a) and leached (b) graphite.

Composition, structure, and morphology of LNMO spinel

The mixed oxide shows a cubic spinel structure, the XRD pattern of which can be indexed in the Fd3m space group, as no peaks of the superstructure indexable in a space group of $P4_332$ were detected (see Fig. 4a). In other words, it has a disordered structure with Ni and Mn located randomly on the octahedral sites formed by the oxygen cubic packing. This behaviour is consistent with the synthesis conditions as the ordered structure formation is usually obtained after a re-annealing process.[44] The pattern also shows weak peaks assignable to the Li_xNiO phase, which suggests the presence of a small content of Mn^{3+} in the spinel structure.

The morphology of LNMO was examined by SEM, as shown in Fig. 4b. Most of the particles exhibit a well-defined polyhedral morphology, with a tendency to adopt an octahedral shape when their size increases. The synthesis method used does not facilitate the growth of the particles in the form of truncated octahedrons, so the {111} planes would be the most exposed to interact with the reagents.[45] Particle size is heterogeneous though the particles of submicron size predominate.

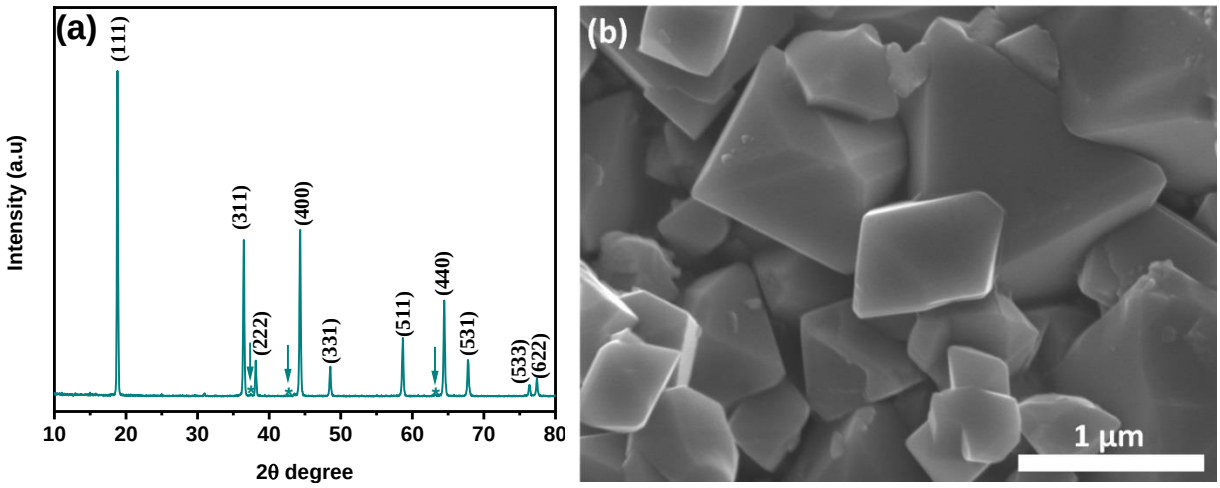

Figure 4. XRD pattern (a) and SEM image (b) of spinel $LiNi_{0.5}Mn_{1.5}O_4$.

The Mn/Ni atomic ratio of the spinel was determined by two different techniques: EDS and XRF. The EDS spectrum of one of the regions analyzed is shown in Figure S6a. As expected, most elements are Mn, O, and Ni, while Cl is in the form of traces. The mapping of the main elements

(Fig. S6 b) confirms their homogeneous distribution. Table S1 shows the averaged composition values of the ten observed regions of the sample holder, together with those obtained from XRF. Traces of other elements, not observed by EDS (Al, Fe, and Si) were also detected by this technique, but the content was insignificant. These techniques yielded different values for the Mn/Ni atomic ratio, 4.43 and 3.16, by EDS and XRF, respectively. The latter value is slightly higher than that corresponding to the stoichiometric formula. Determining light elements by XRF and EDS is difficult, and in the case of Li it is practically impossible because the emitted radiations in both cases are characterized by extremely low energy and long-wavelength. This is one of the deficiencies of both techniques in accurately determining the composition of the compound. The high deviation of the EDS measures is consistent with other reports on this spinel, where the values of the Mn/Ni ratio can range between 0.2 and 5.6, affecting the particle morphology, among other factors.[46,47] The impurities of the mixed Li-Ni oxide would lower the Ni content in the spinel.

The surface structure of the spinel was investigated by XPS measurements. Fig. 5a and b shows the Mn 2p and Ni 2p photoemission spectra. The two peaks of Mn spectrum ($2p_{3/2}$ and $2p_{1/2}$) (Fig. 5a) are rather symmetric and their binding energies, 642.6 and 654.1 eV, are consistent with Mn^{4+}.[48] Nevertheless, the Mn signal is often fitted to two components (Mn^{3+} and Mn^{4+})[49–52] but the relative contribution of both valences is very irregular, with contents of Mn^{3+} between about 50% [50–52] to scarcely 10% (the latter value being more consistent with the composition of the spinel).[49] These discrepancies result from the small difference in the binding energies of these two valences. Changes in the models used to fit the profile would be responsible for these differences, which are otherwise difficult to reconcile with the results obtained by other measures, both analytical and electrochemical ones. We doubt the meaning of the convolution of the Mn signal and, therefore, discarded it. The Ni 2p spectrum exhibits four peaks, two of them at 855.0 and 872.5 eV assigned to Ni $2p_{3/2}$ and Ni $2p_{1/2}$, respectively. These values are consistent with Ni^{2+} ions at octahedral sites in the spinel structure,[53] although the presence of a minor amount of Ni^{3+} is not ruled out.[54]

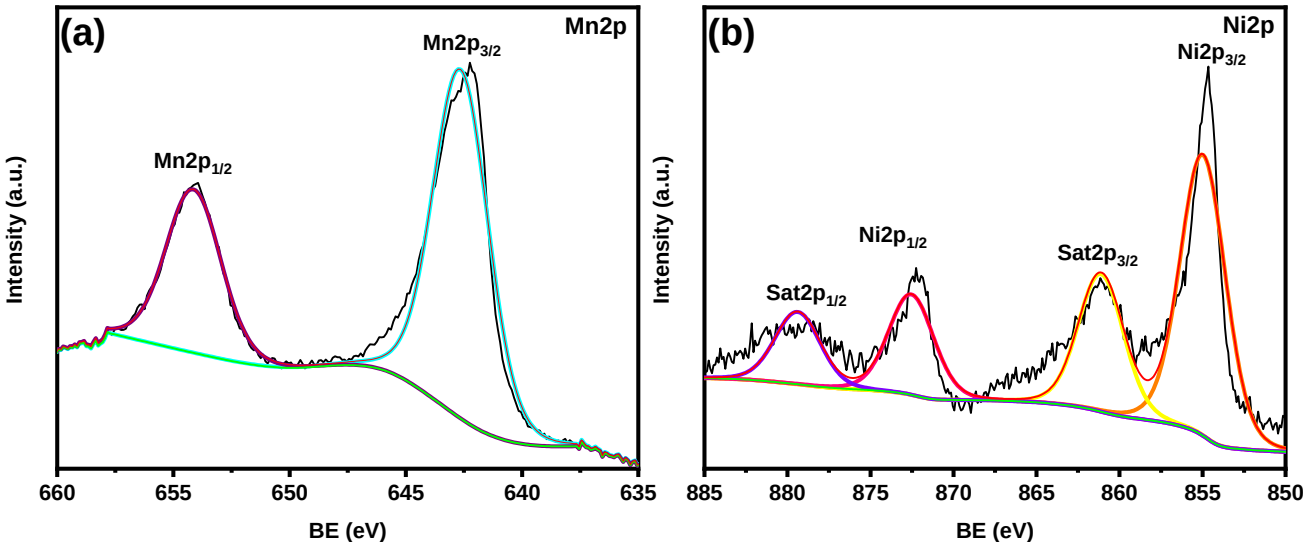

Figure 5. Photoemission peak of (a) Mn 2p and (b) Ni 2p of spinel $LiNi_{0.5}Mn_{1.5}O_4$.

Electrochemical properties

Half-cells of Graphite

The electrochemical properties of the two systems, the spinel and the recovered graphite, were studied under galvanostatic regime. These properties were measured in two cell types: half cells and full cells. Some of the discharge/charge curves recorded for the graphite in half cells at 0.2 C rate (74 mA g^{-1}) are shown in Fig. 6a. The first discharge curve exhibits a rapid drop in the potential, followed by a pseudo plateau between 0.8 - 0.7 V and a smoother decrease of the potential until 0.0 V is reached. The small plateau is assigned to the formation of the solid electrolytic interface (SEI) on the surface of graphite particles.[55] In commercial graphite, such as MCMB, the length of this plateau is slightly shorter than that observed here.[37] The SEI formation in the recovered graphite can be due to an increase in both surface delamination and the content of defects caused during the life of the spent batteries and the leaching process. The presence of impurities, especially those from the battery components (P, Fe, Co, Ni, Cu) and leaching (Cl) could also contribute to this process. After the first discharge, the electrode tends to stabilize. When the cell is charged, a slight polarization is observed, followed by a sharp rise at around 0.5 V and the virtual disappearance of

the pseudo-plateau assigned to the SEI formation. It also disappears in second and subsequent discharge curves while the potential decreases smoothly from 1 V. The charge curves hardly change as the cell is cycled. The shape of the discharge/charge curves of the unleached sample is quite similar, with the presence of a pseudo-plateau in the first discharge curve and its disappearance after the first charge process (Fig. S7).

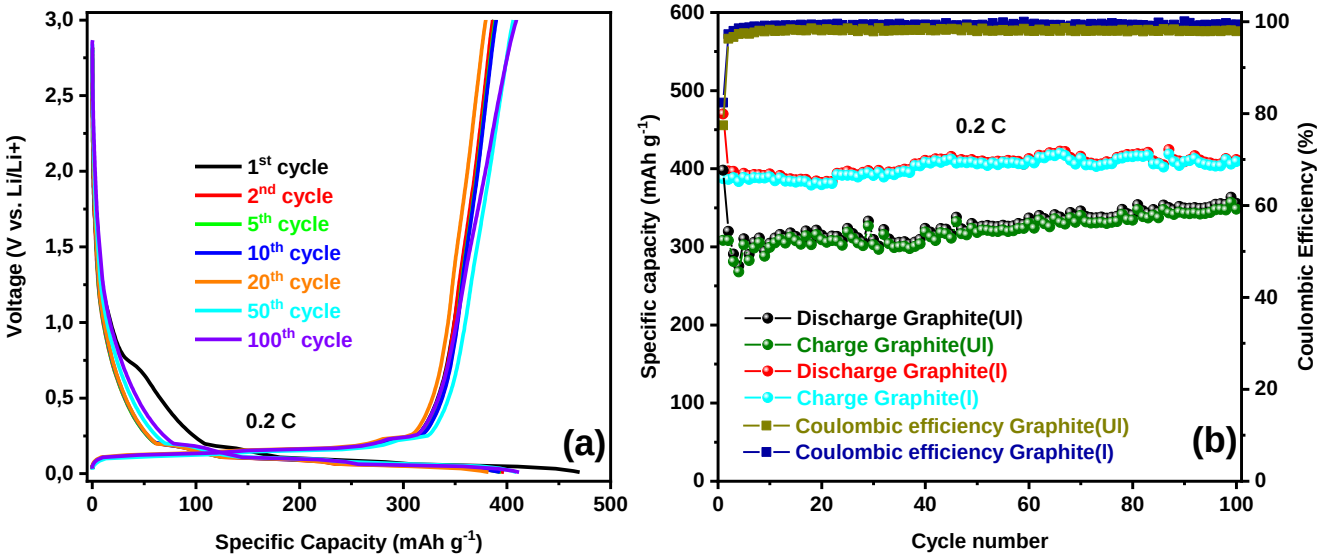

Figure 6. (a) Galvanostatic charge-discharge curves of leached graphite. (b) Specific capacity vs cycle number and coulombic efficiency of unleached and leached graphite. Half-cell configuration. Rate 0.2 C.

Figure 6b shows the values of specific capacity as a function of the number of cycles. After the first cycle, when the cell is more stabilized, the delivered capacity remains virtually constant in the first fifty cycles; then a slight tendency to increase is observed. In the first hundred cycles the average capacity is around 390 mAh g^{-1}, somewhat higher than its theoretical value. The values of the coulombic efficiency begin increasing from 83 % in the first cycle until over 98 % from the first ten cycles. The average capacity values supplied by the unleached graphite, around 300 mAh g^{-1}, are almost 25% lower than those of the leached graphite. The small structural differences between both samples does not seem to be the origin of their different performance. A more plausible cause is the

409 greater amount of impurities present in the unwashed electrode. Moreover, the leached graphite has
410 a lower content of impurities, which are protected by a layer of C, as revealed by the XPS spectrum.
411 This layer can hinder their reactivity and mitigate the negative effects of the secondary reactions in
412 which they participate.

413 To our knowledge, only two articles have described the cycling properties of recycled graphite from
414 spent batteries in Li cells.[28,30] At a current density of 0.2C, the average capacity delivered by the
415 electrode on cycling, as studied by Yang et al.[28], was around 500 mAh g^{-1}, 25 % higher than that
416 measured in our graphite. Different models were used by these authors to explain this "abnormal"
417 capacity associated with particle and pore size. However, the value of the BET surface, barely 2 m^2
418 g^{-1}, a value within the experimental error of the technique, questions this explanation. In addition,
419 the absence of the plateau associated with the SEI makes this explanation less convincing. The
420 properties of the recovered graphite in prolonged cycling were measured at a current density of 1C.
421 The average capacity after 100 cycles was 166 mAh g^{-1}, more consistent with the usual behavior of
422 graphite. Other features that could affect graphite performance, such as the impurities of the battery
423 components and the structural disorder that can affect the SEI formation and the lithium insertion
424 mechanism, were not considered.

425 An average discharge capacity value of 374 mAh g^{-1}, very close to the theoretical value of graphite,
426 has been reported by Rothermel et al.[30] for the graphite originating from a LIB cycled to 70 %
427 SOH (aged graphite) and cycled for 100 cycles at 0.5C with a previous activation at 0.1C. The
428 behavior of this graphite serves as a reference to be contrasted with our results. After electrolyte
429 extraction with subcritical and supercritical CO_2, the average discharge capacity values were 380
430 and 345 mAh g^{-1}, respectively. Without undermining the commendable effort made by the authors
431 to relate the performance of the recovered graphite with its content of impurities and degree of
432 crystallinity, we consider that the origin of the observed behavior is unclear. Obviously, both
433 extraction methods decrease the impurity content of graphite, but the capacity values vary

randomly. Besides, the degree of crystallinity of the graphite, deduced from the values of L_a, is not consistent with the sequence of capacity values. Both extraction processes increase the value of L_a, from 175 to 635 (sb CO_2) and 800 nm (sp CO_2) nm. However, this apparent improvement in crystallinity, more pronounced when the extraction is carried out under supercritical conditions, does not lead to an improvement in the electrode performance but worsens it in a significant way.

Half-cells of LNMO Spinel

The charge/discharge curves of the $LiNi_{0.5}Mn_{1.5}O_4$ spinel, recorded between 3.5 and 4.9 V and at 0.2 C (29.4 mA g^{-1}), are shown in Fig. 7a. The Li^+ removal occurs essentially in two stages centered at ca. 4.7 V and assigned to the oxidation of Ni^{2+} to Ni^{4+}. The small plateau detected around 4.2 V is assigned to the oxidation of a small fraction of Mn^{3+} to Mn^{4+}, which means a slight deviation from the stoichiometric formula (barely 5 % considering the theoretical capacity, 147 mAh g^{-1}). The capacity value of the first charge, ca. 153 mAh g^{-1}, is slightly higher than the theoretical one. When the cell is discharged, a significant decrease in capacity is observed, ca. 113 mAh g^{-1}, and this value decreases slowly in subsequent cycles. After 100 cycles, the average value of the average capacity is around 100 mAh g^{-1}. This value is somewhat lower than that measured by Chemelewski et al.[56] around 120 mAh g^{-1} in octahedral particles synthesized at 900 ºC and post-annealed at 700 ºC, using $LiOH{\cdot}H_2O$ as Li source. Note that many factors affect the electrochemical performance of this spinel, such as cation ordering, particle size and morphology, among others. Even obvious discrepancies need to be clarified. For example, Manthiram et al.[57] found that the best electrochemical properties are observed in well-defined octahedral particles and, by contrast, the worst ones are shown in truncated octahedron particles. In a more recent study, Liu et al. reached the opposite conclusion.[58]

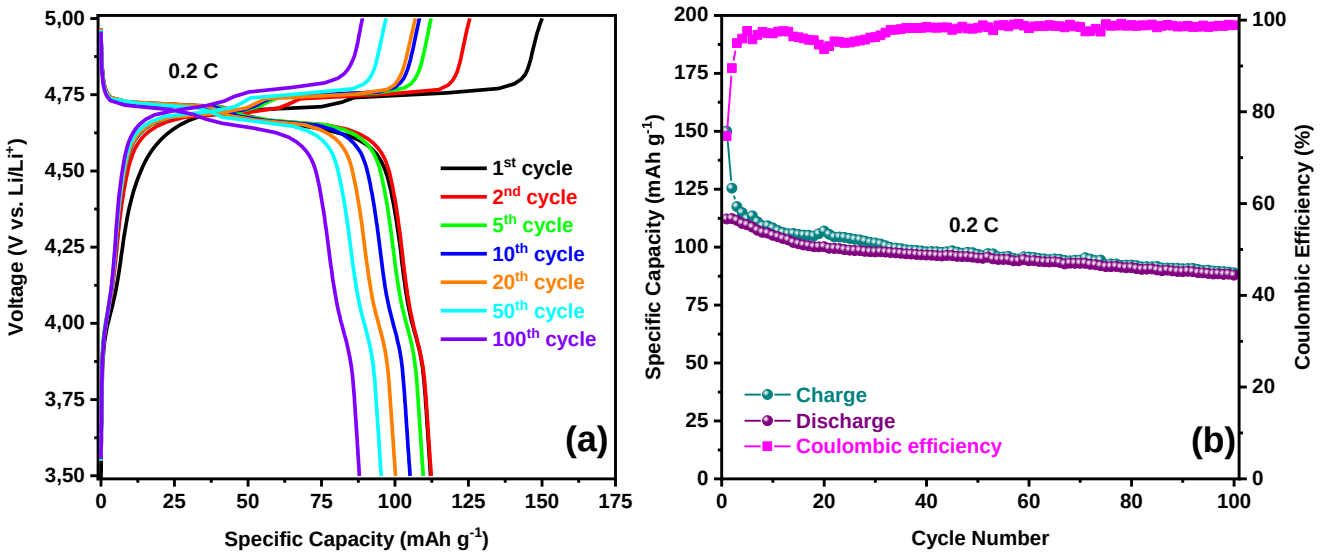

Figure 7. (a) Galvanostatic charge-discharge curves of $LiNi_{0.5}Mn_{1.5}O_4$. (b) Specific capacity vs cycle number and coulombic efficiency. Half-cell configuration Rate: 0.2 C.

Full cells LIB

Leached graphite was used as the negative electrode for full cells because it showed better electrochemical performance compared with unleached graphite in a half-cell configuration. The capacity values of leached graphite and LNMO spinel measured in half cells were taken as a reference to ensure that the capacity ratio of the negative electrode (N) to the positive electrode (P) (N/P ratio) was next to 1. Since the capacities were around 100 and 400 mAh g^{-1}, for spinel and graphite, respectively, the spinel/graphite ratio was 4: 1 (by weight). Some charge/discharge curves of this cell cycled between 3.5 and 5.0 V and at 0.1C (related to the spinel) are shown in Fig. 8a. The profile shapes are somewhat different and more complex than those measured for the spinel in a half-cell configuration (Fig. 7a) since the two stages of oxidation from Ni^{2+} to Ni^{4+} are not well defined. The explanation for this behavior would require the use of additional tools, such as a three-electrode cell, to simultaneously measure the LNMO/Li and graphite/Li charge/discharge curves. This experiment is beyond the objectives of this work, which focused on the ability of recycled graphite in this type of batteries. Besides, the overcharge observed in this configuration is lower than that observed in a half-cell configuration, and in the first cycle the efficiency approaches 90 %.

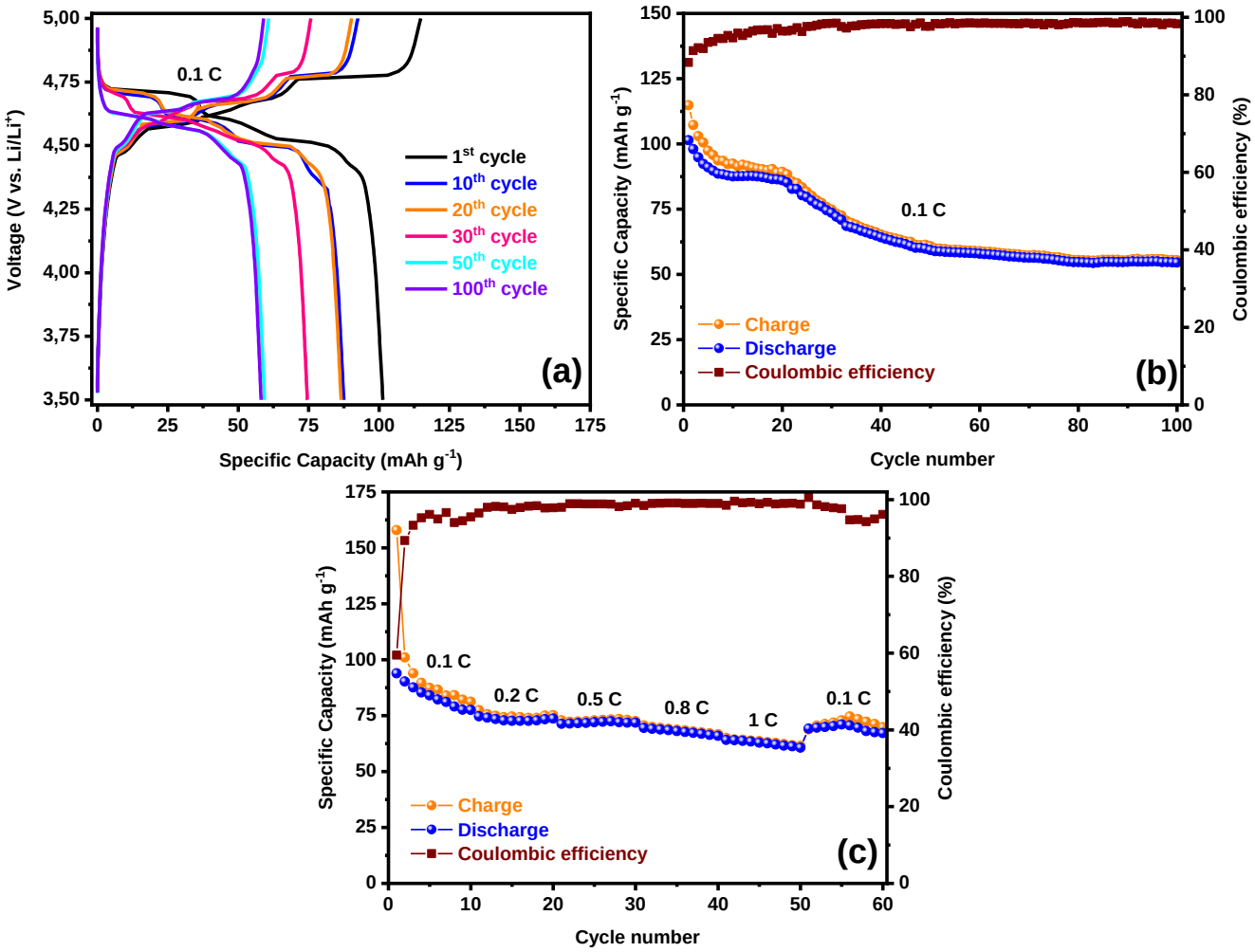

474

475 **Figure 8**. (a) Charge-discharge curves of leached graphite/ $LiNi_{0.5}Mn_{1.5}O_4$ full-cell. (b) Specific
476 capacity vs cycle number and coulombic efficiency. Rate: 0.1 C. (c) Rate capability. The specific
477 capacity and rate are referred to the spinel.

478 The cycling performance of the cell is shown in Fig. 8b. Four sections can be distinguished in the
479 curve representing the capacity delivered by the cell. In the first ten cycles, a pronounced decrease,
480 from 102 to 88 mAh g^{-1}, is observed. In the next ten cycles, the fall stops, which shows a good
481 capacity retention. As the cycling progresses, the capacity decreases again but in a softer way; in
482 cycle 50 the capacity is around 63 mAh g^{-1}. In the last stage, until the 100 cycles are completed, the
483 capacity decreases very slowly, stabilizing at an average value of about 60 mAh g^{-1}. Regarding the
484 evolution of the coulombic efficiency, in the first third of the cycle, the tendency is to increase
485 progressively from 90 % to 98 %, a value that is maintained with slight fluctuations until the end of

the measurement. The complex profiles of the charge/discharge curves are maintained in the different cycles measured (Fig. 7a).

The rate capability results of the cell at 0.1, 0.2, 0.5, 0.8, and 1C, ten cycles for each rate, are shown in Fig. 8c. At 0.1C, the behavior is similar to that found in a prolonged cycling test, a pronounced decrease in capacity in the first cycles, with a tendency to stabilize in the last cycles. This stability is manifested at higher speeds, with an average value at 0.2 and 0.5 C ca. 73 and 70 mAg g^{-1}, respectively. For rates 0.8 and 1C, a somewhat more pronounced drop is observed in the delivered capacity, with values ca. 68 and 62 mAh g^{-1}, respectively. When returning to 0.1C, the capacity of the cell increases, reaching an average value ca. 75 mAh g^{-1}, like that observed at the end of the first stage of the measurement.

Several factors cause capacity loss during cycling, but one in particular affects the stability of the $LiPF_6$ electrolyte when operating at high voltages. The salt can undergo decomposition in LiF and PF_5. The latter halide reacts quickly with traces of moisture releasing HF, which dissolves part of the cations of the compound:[59]

$$2\ LiNi_{0.5}Mn_{1.5}O_4 + 4HF \rightarrow 3\ Ni_{0.25}Mn_{0.75}O_2 + 0.25\ NiF_2 + 0.5\ MnF_2 + 2\ LiF + 2\ H_2O \quad (5)$$

The dissolved transition metal ions can migrate to the anode through the separator and be reduced on its surface or can interact with the lithiated graphite, according to the following reaction:[60]

$$Mn^{2+} + 2LiC_6 \rightarrow Mn + 2Li^{+} + \text{graphite} \quad (6)$$

These reactions may be especially favored in the "fresh" spinel, that is, in the first cycles of battery operation. As reactions (5) and (6) progress, the thickness of the products formed will grow by acting as a protective layer on the active particle and slowing down its structural deterioration. In fact, the electrode coated with a protective layer of Al_2O_3 led to much better capacity retention. The coating of graphite is particularly outstanding as it may hinder the Mn deposition and mitigate reaction (5) as a result.[61] Different strategies have been used to modify the composition of the

electrolyte. The simplest one is the substitution of $LiPF_6$ salt by $LiB(C_2O_4)_2$ with the resulting elimination of HF formation.[62] The model named "multilayer electrolyte cell" is more complex as it consists of two liquid electrolytes separated by a solid electrolyte.[63] In both cases, better capacity retention was observed. Here, we used a conventional electrolyte without considering the proposed alternatives to improve cell performance, in agreement with our main objectives, namely the recovery of graphite from spent batteries and the β-spodumene mineral as Li source.

The performance of the proposed full-cell model was compared with that of other full cells reported in the literature, made from the same components but from more conventional sources. In this sense, the abundant number of articles reporting on the spinel LNMO in a half-cell configuration–four reviews [64–66] citing an enormous number of articles–contrasts with the small number of studies on a full-cell configuration so far reported, to our knowledge fewer than ten. Table 3 shows some properties related to the performance of these cells, including a column with the capacity ratio, N/P, a parameter that is not usually included in scientific publications although its importance is undeniable. The ideal value of this parameter would be 1. In general, the rates used in prolonged cycling are usually slow, mostly around 0.1C, except for those in references [68] and [69], where a rate of 0.5C was used. The origin of this low rate is the slowness of the extraction and insertion of Li from the spinel and the limited availability of Li, which further hinders the kinetics of the electrochemical process. All the cells collected show a loss of the delivered capacity when cycling. The capacity loss per cycle ranges from 0.1 to 3.9 mAh g^{-1}. Our cell only lost 0.4 mAh g^{-1}, a value that reflects a good performance, only surpassed by one of the nine cells described in the literature.[67] It is worth pointing out that the process of the spinel synthesis studied by Kim et al.[68] presents important differences with respect to the process studied in this work. First, the Li source is the commercial Li_2CO_3, which is more expensive than LiCl. Second, it uses four heating stages that are extended for longer periods: 500 °C, 12 h; 650 °C, 12 h; 900 ºC, 6h and an annealing at 700 ºC 48 h. These differences reveal the superiority of our process in terms of cost effectiveness and

energy savings. In a half-cell configuration, the capacity released by the spinel is also higher, 120 mAh g^{-1} at 100 cycles and at a rate of 0.2C. Moreover, the rate capability test was not carried out in any of the references included in Table 3. The capacity values obtained at 0.5C, 70 mAh g^{-1} (Fig. 8c) are comparable to those of Sahoo et al.[45,69] in pouch-type cells and higher than those of Pieczonka et al.[67]

In this context, it is interesting to highlight the results of the electrochemical behavior of recycled graphite reported by Rothermel et al.,[30] also obtained in a full-cell configuration, using as a source of Li, $LiMn_{1/3}Co_{1/3}Ni_{1/3}O_2$, the cathode material of the battery from which graphite was extracted. This aged graphite exhibits somewhat good capacity retention, capacity loss over 100 cycles ca. 0.3 mAh g^{-1} obtained at 1C, with a previous activation at 0.2C. The best features of this cell are not surprising since it was cycled between 1.7 and 4.25 V. In addition, the compound has a 2D structure whose intercalation/deintercalation kinetics of Li^+ is more favorable than that in the 3D structure of the spinel.

Table 3. Selected properties of $LiNi_{0.5}Mn_{1.5}O_4$//Graphite full cells reported in the literature

C_i[a]	C_f[a]	Cycle number	C. L.[b]	Rate (C)	N/P	Graphite	Ref
96	33	40	1.6	0.08	0.7	MCMB	[62]
84	25	15	3.9	0.05	---	MCMB	[63]
70	37	100	0.3	0.07	---	Commercial	[61]
82	40	100	0.4	0.1	---	MCMB	[60]
97	50	100	0.5	0.08	---	MCMB	[59]
110	60	50	1.0	0.13	---	Commercial	[57]
105	85	200	0.1	0.2	1.05	Commercial	[68]
116	58	80	0.7	0.5	---	Powder	[67]
88[c]	69	50	0.4	0.5	0.86	MCMB	[45,69]
100	60	100	0.4	0.1	1.02	Recycled	This work

[a] C_i and C_f: initial and final capacity, respectively, in mAh g^{-1}. [b] Capacity loss per cycle, mAh g^{-1}. [c] Pouch cell

Finally, some concluding remarks regarding the economic performance of the proposed laboratory scale process to fabricate electrode materials are revealed:

- The starting material for the recycling of graphite is close to what may occur in real waste because it is made up of spent graphite from different spent LIBs provided by many end consumers.
- Although the process involves calcination steps in both synthesis and recycling graphite, the energy consumption is minimized because the periods of reaction are rather short, 1 and 2 h, respectively. Furthermore, laboratory results demonstrated that both treatments can be carried out in the same furnace. For the next scale either pilot or commercial, a fluidized bed reactor could be the more adequate equipment to carry out both processes.[70]
- The operation of filtration is another common operation for both processes. In the laboratory, the same filter was used for both processes. In an actual process the appropriate equipment could be a rotary vacuum-drum filter.
- The separation of the spent graphite from the cupper foil is very simple because involves a one-step sieving in comparison with others that required and additional step of crushing.[3]

Conclusions

In this work, graphite was recovered from spent Li-ion batteries dismantled manually. It was purified in two simple steps, by heating in an inert atmosphere at a moderate temperature (450 °C), followed by leaching with diluted HCl (3M). Although this treatment does not fully eliminate the impurities of the recovered graphite, it drastically reduces them, as evidenced by both the compositional measures performed by different analytical techniques and the ash content when calcined in an O_2 atmosphere, less than 0.5 %. The crystallinity of the recycled graphite is not affected by the leaching treatment and is very similar to that of commercial graphite, evaluated from the broadening of the X-ray diffraction peaks and the relative intensities of the I_D and I_G Raman

vibration bands. Although not the main objective of this work, we do draw attention to the difficulty in making both types of measures compatible, given the different principles on which both characterization techniques are based. However, the cleaning treatment of graphite does affect its electrochemical properties significantly, showing a better performance compared with the unleached graphite. Therefore, impurities are the main cause of the deterioration of the electrochemical properties. Only after leaching is the specific capacity value close to the theoretical one.

To approach a more realistic application in terms of the reuse of recycled graphite, its electrochemical behavior was also investigated in a full-cell configuration. We chose the LNMO spinel as a cathode material able to operate at voltages close to 5 V, as opposed to Li metal. For its synthesis, a low-cost procedure was applied, using Li extracted from spodumene, a raw material available in large deposits in Argentina, and through thermal treatment in a single step at 800 °C. The performance of this more realistic battery is comparable to the best results reported in similar batteries prepared with commercial graphite. It is worth mentioning its good behavior in the rate capability test. Unfortunately, for this type of measure, we have not found bibliographic references to establish comparisons. After the first cycles at low current densities (0.1C) in which a continuous decrease in the specific capacity is observed, the cell tends to stabilize. Then, the average specific capacity up to a rate of 1C decreases very slowly, and the coulombic efficiency is close to 100 % at the different rates used.

Acknowledgments

This research was funded by Ministerio de Economía y Competitividad (Project MAT2017-87541-R) and Junta de Andalucía (Group FQM-175).

References

[1] S. Al-thyabat, T. Nakamura, E. Shibata, A. Iizuka, *Miner. Eng.* **2013**, *45*, 4–17.

[2] M. Jacoby, *Chem. Eng. News* **2019**, *97*.

[3] F. Y. Yao Lu, Yao Haisen, Xi Guoxi, *RSC Adv.* **2016**, *6*, 17947–17954.

[4] S. Goriparti, E. Miele, F. De Angelis, E. Di, R. Proietti, C. Capiglia, *J. Power Sources* **2014**, *257*, 421–443.

[5] A. Mayyas, "Are there enough materials to cover li-ion batteries?," can be found under https://www.manufacturingcleanenergy.org/blog-20180815.html, **2018**.

[6] B. Huang, Z. Pan, X. Su, L. An, *J. Power Sources* **2018**, *399*, 274–286.

[7] W. Zhang, C. Xu, W. He, G. Li, J. Huang, *Waste Manag. Res.* **2018**, *36*, 99–112.

[8] W. Lv, Z. Wang, H. Cao, Y. Sun, Y. Zhang, Z. Sun, *ACS Sustain. Chem. Eng.* **2018**, *6*, 1504−1521.

[9] L. Li, X. Zhang, M. Li, R. Chen, F. Wu, K. Amine, J. Lu, *Electrochem. Energy Rev.* **2018**, *1*, 461–482.

[10] C. Liu, J. Lin, H. Cao, Y. Zhang, Z. Sun, *J. Clean. Prod.* **2019**, *228*, 801-813.

[11] B. Moradi, G. G. Botte, *J. Appl. Electrochem.* **2016**, *46*, 123–148.

[12] M. Geissdoerfer, P. Savaget, N. M. P. Bocken, E. Jan, *J. Clean. Prod.* **2017**, *143*, 757–768.

[13] A. K. Haridas, C. S. Sharma, T. N. Rao, *Electrochim. Acta* **2016**, *212*, 500–509.

[14] J. C. Arrebola, A. Caballero, L. Hernán, J. Morales, **2010**, *195*, 4278–4284.

[15] M. Börner, P. Niehoff, B. Vortmann, S. Nowak, M. Winter, F. M. Schappacher, *Energy Technol.* **2016**, *4*, 1631–1640.

[16] X. Y. Feng, C. Shen, X. Fang, C. H. Chen, *J. Alloys Compd.* **2011**, *509*, 3623–3626.

[17] T. Kazda, J. Vondrák, M. Sedlarikova, J. Tichý, P. Čudek, *ECS Trans.* **2016**, *74*, 199–204.

[18] K. Cao, T. Shen, K. Wang, D. Chen, W. Wang, *Ceram. Int.* **2017**, *43*, 8694–8702.

[19] X. Fang, C. Shen, M. Ge, J. Rong, Y. Liu, A. Zhang, F. Wei, C. Zhou, *Nano Energy* **2015**,

626 *12*, 43–51.
627 [20] K. Lee, G. J. Yang, Y. Kim, *Ceram. Int.* **2017**, *43*, 15510–15518.
628 [21] L. Li, J. Sui, J. Chen, Y. Lu, *Electrochim. Acta* **2019**, *305*, 433–442.
629 [22] T. Mei, W. Pi, L. Zhang, J. Wang, J. Li, X. Wang, *Mater. Lett.* **2016**, *173*, 141–144.
630 [23] R. Qiao, Y. Wang, P. Olalde-Velasco, H. Li, Y. S. Hu, W. Yang, *J. Power Sources* **2015**,
631 *273*, 1120–1126.
632 [24] L. Wang, D. Chen, J. Wang, G. Liu, W. Wu, G. Liang, *Powder Technol.* **2016**, *292*, 203–
633 209.
634 [25] H. Zhao, F. Li, X. Shu, J. Liu, T. Wu, Z. Wang, Y. Li, J. Su, *Ceram. Int.* **2018**, *44*, 20575–
635 20580.
636 [26] L. I. Barbosa, J. A. González, C. Ruiz, *Thermochim. Acta* **2015**, *605*, 63–67.
637 [27] Y. Guo, F. Li, H. Zhu, G. Li, J. Huang, W. He, *Waste Manag.* **2016**, *51*, 227–233.
638 [28] Y. Yang, S. Song, S. Lei, W. Sun, H. Hou, F. Jiang, X. Ji, *Waste Manag.* **2019**, *85*, 529–537.
639 [29] J. E. C. Sabisch, A. Anapolsky, G. Liu, A. M. Minor, *Resour. Conserv. Recycl.* **2018**, *129*,
640 129–134.
641 [30] S. Rothermel, M. Evertz, J. Kasnatscheew, X. Qi, M. Grützke, M. Winter, S. Nowak,
642 *ChemSusChem* **2016**, *9*, 3473–3484.
643 [31] C. Hanisch, T. Loellhoeffel, J. Diekmann, K. J. Markley, W. Haselrieder, A. Kwade, *J.*
644 *Clean. Prod.* **2015**, *108*, 301–311.
645 [32] D. Di Lecce, L. Carbone, V. Gancitano, J. Hassoun, *J. Power Sources* **2016**, *334*, 146–153.
646 [33] A. Benítez, Á. Caballero, E. Rodríguez-Castellón, J. Morales, J. Hassoun, *ChemistrySelect*
647 **2018**, *3*, 10371–10377.
648 [34] J. F. Moulder, W. F. Stickle, P. E.'Sobol, K. D. Bomben, *Handbook of X-Ray Photoelectron*
649 *Spectroscopy*, Perkin-Elmer Corporation, **1992**.
650 [35] S. Leroy, F. Blanchard, R. Dedryvère, H. Martinez, B. Carré, D. Lemordant, D. Gonbeau,

651 *Surf. Interface Anal.* **2005**, *37*, 773–781.
652 [36] Ó. Vargas, Á. Caballero, J. Morales, E. Rodríguez-Castellón, *ACS Appl. Mater. Interfaces*
653 **2014**, *6*, 3290–3298.
654 [37] J. C. Arrebola, A. Caballero, L. Hernán, J. Morales, *J. Electrochem. Soc.* **2009**, *156*, 986–
655 992.
656 [38] R. Krishna, J. Wade, A. N. Jones, M. Lasithiotakis, P. M. Mummery, B. J. Marsden, *Carbon*
657 *N. Y.* **2017**, *124*, 314–333.
658 [39] H. P. Klug, L. E. Alexander, *X-Ray Diffraction Procedures for Polycrystalline and*
659 *Amorphous Materials*, **1974**.
660 [40] M. S. Seehra, A. S. Pavlovic, *Carbon N. Y.* **1993**, *31*, 557–564.
661 [41] A. Milev, M. Wilson, G. S. K. Kannangara, N. Tran, *Mater. Chem. Phys.* **2008**, *111*, 346–
662 350.
663 [42] L. G. Caņado, K. Takai, T. Enoki, M. Endo, Y. A. Kim, H. Mizusaki, A. Jorio, L. N. Coelho,
664 R. Magalhães-Paniago, M. A. Pimenta, *Appl. Phys. Lett.* **2006**, *88*, 1–4.
665 [43] O. A. Maslova, M. R. Ammar, G. Guimbretière, J. N. Rouzaud, P. Simon, *Phys. Rev. B -*
666 *Condens. Matter Mater. Phys.* **2012**, *86*, 1–5.
667 [44] J. Song, D. W. Shin, Y. Lu, C. D. Amos, A. Manthiram, J. B. Goodenough, *Chem. Mater.*
668 **2012**, *24*, 3101–3109.
669 [45] K. Sahoo, J. Majhi, A. Mitra, A. S. Kumar, S. B. Majumder, *J. Electrochem. Soc.* **2019**, *166*,
670 A342–A352.
671 [46] S. Yang, D. O. Schmidt, A. Khetan, F. Schrader, S. Jakobi, M. Homberger, M. Noyong, A.
672 Paulus, H. Kungl, R. A. Eichel, et al., *Materials (Basel).* **2018**, *11*, 1–19.
673 [47] J. Cabana, F. O. Omenya, N. A. Chernova, D. Zeng, M. S. Whittingham, C. P. Grey, **2012**.
674 [48] F. Luna-Lama, C. Hernández-Rentero, A. Caballero, J. Morales, *Electrochim. Acta* **2018**,
675 *292*, 522–531.

[49] T. Yang, N. Zhang, Y. Lang, K. Sun, *Electrochim. Acta* **2011**, *56*, 4058–4064.

[50] Y. Xue, Z. Wang, L. Zheng, F. Yu, B. Liu, Y. Zhang, K. Ke, *Sci. Rep.* **2015**, *5*, 1–11.

[51] C. Yin, H. Zhou, Z. Yang, J. Li, *ACS Appl. Mater. Interfaces* **2018**, *10*, 13624–13634.

[52] T. Gu, J. Wang, J. H. Tian, X. Zheng, K. Lu, Y. Xin, H. Wang, R. Yang, *ChemElectroChem* **2019**, *6*, 2224–2230.

[53] J. C. Arrebola, A. Caballero, M. Cruz, L. Hernán, J. Morales, E. R. Castellón, *Adv. Funct. Mater.* **2006**, *16*, 1904–1912.

[54] R. Tenne, A. Wold, A. P. Lett, K. Amine, H. Tukamoto, H. Yasuda, Y. Fuiita, **1996**, *143*, 1607–1613.

[55] J. Yao, G. X. Wang, J. H. Ahn, H. K. Liu, S. X. Dou, *J. Power Sources* **2003**, *114*, 292–297.

[56] K. R. Chemelewski, D. W. Shin, W. Li, A. Manthiram, *J. Mater. Chem. A* **2013**, *1*, 3347–3354.

[57] A. Manthiram, K. Chemelewski, E. S. Lee, *Energy Environ. Sci.* **2014**, *7*, 1339–1350.

[58] H. Liu, X. Zhang, X. He, A. Senyshyn, A. Wilken, D. Zhou, O. Fromm, P. Niehoff, B. Yan, J. Li, et al., *J. Electrochem. Soc.* **2018**, *165*, A1886–A1896.

[59] N. P. W. Pieczonka, Z. Liu, P. Lu, K. L. Olson, J. Moote, B. R. Powell, J. Kim, *J. Phys. Chem. C* **2013**, *117*, 15947–15957.

[60] J. H. Kim, N. P. W. Pieczonka, Z. Li, Y. Wu, S. Harris, B. R. Powell, *Electrochim. Acta* **2013**, *90*, 556–562.

[61] X. Xiao, D. Ahn, Z. Liu, J. H. Kim, P. Lu, *Electrochem. commun.* **2013**, *32*, 31–34.

[62] J. C. Arrebola, A. Caballero, L. Hernán, J. Morales, *J. Power Sources* **2008**, *183*, 310–315.

[63] N. Mahootcheianasl, J. H. Kim, N. P. W. Pieczonka, Z. Liu, Y. Kim, *Electrochem. commun.* **2013**, *32*, 1–4.

[64] C. M. Julien, A. Mauger, *Review of 5-V Electrodes for Li-Ion Batteries: Status and Trends*, **2013**.

[65] X. L. Xu, S. X. Deng, H. Wang, J. B. Liu, H. Yan, *Nano-Micro Lett.* **2017**, *9*, 22.

[66] W. Li, B. Song, A. Manthiram, *Chem. Soc. Rev.* **2017**, *46*, 3006–3059.

[67] N. P. W. Pieczonka, V. Borgel, B. Ziv, N. Leifer, V. Dargel, D. Aurbach, J. H. Kim, Z. Liu, X. Huang, S. A. Krachkovskiy, et al., *Adv. Energy Mater.* **2015**, *5*, 1501008.

[68] J. H. Kim, N. P. W. Pieczonka, P. Lu, Z. Liu, R. Qiao, W. Yang, M. M. Tessema, Y. K. Sun, B. R. Powell, *Adv. Mater. Interfaces* **2015**, *2*, 1–13.

[69] K. Sahoo, G. D. Prasad, K. Jagdish, A. Srinivas Kumar, S. B. Majumder, *Trans. Indian Inst. Met.* **2019**, 1-13.

[70] P. Hayes, E. Jak, *Introduction to Metallurgical Processing*, Elsevier Ltd., **2014**.

ToC

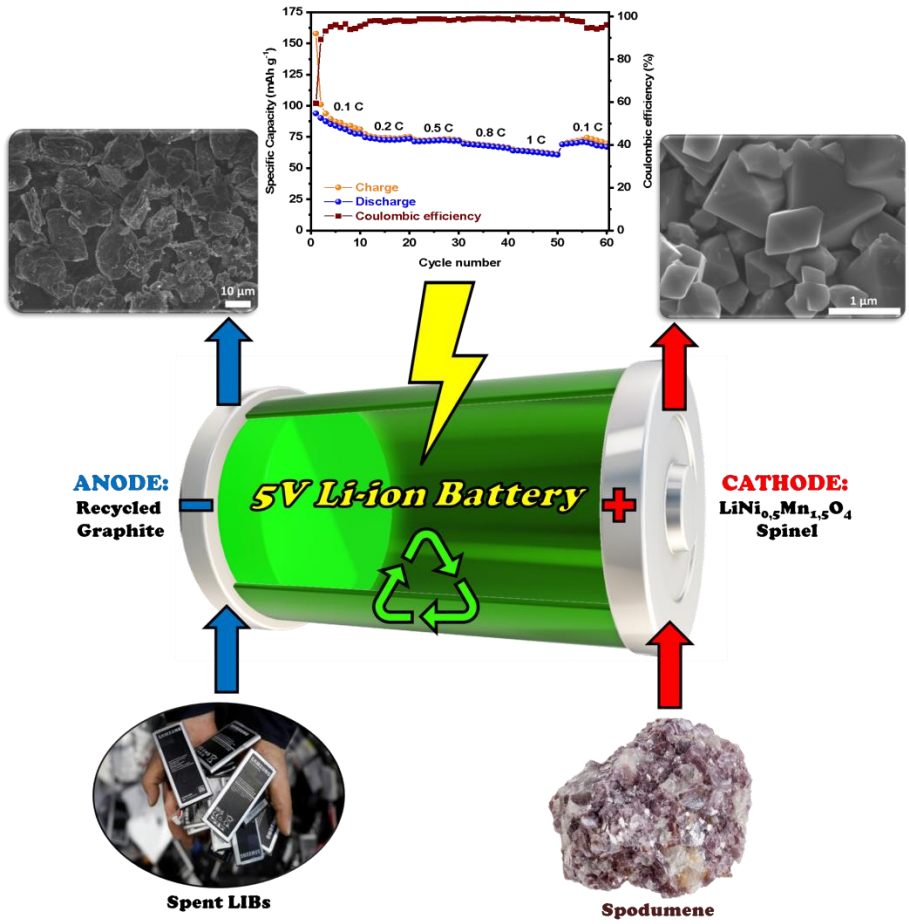
Specific Capacity (mAh g⁻¹)
Coulombic efficiency (%)
Cycle number
0.1 C
0.2 C
0.5 C
0.8 C
1 C
0.1 C
Charge
Discharge
Coulombic efficiency
10 µm
1 µm
ANODE:
Recycled
Graphite
5V Li-ion Battery
CATHODE:
LiNi0,5Mn1,5O4
Spinel
Spent LIBs
Spodumene